Title

Laser ultrasonic imaging of wavefield spatial gradients for damage detection

Journal

Structural Health Monitoring, 20(3)

ISSN

1475-9217

Authors

Wu, Zihan
Chong, See Yenn
Todd, Michael D

Publication Date

2021-05-01

DOI

10.1177/1475921720951336

Peer reviewed

Laser Ultrasonic Imaging of Wavefield Spatial Gradients for Damage Detection

Journal Title
XX(X):1–17

DOI: 10.1177/ToBeAssigned
www.sagepub.com/
SAGE

Zihan Wu, See Yenn Chong, and Michael D Todd*

Abstract

This paper describes a new damage visualization method to investigate and analyze propagating guided Lamb waves using analyses of wavefield spatial gradients. A laser ultrasonic interrogation system (LUIS) was used to create full-field ultrasonic data measurements for ultrasonic wavefield imaging (UWI). The laser scanning process was performed based on both a raster scan and a circle scan. From the high-resolution wavefield data, a spatial gradient-based image processing technique was developed using gradient vectors to extract features sensitive to defects. Local impedance changes at the damaged area would result in a local distortion of the waveform which was captured and quantified by the variation of the gradient vectors in the scanning area as time evolves. Such variation was accumulated over time with a statistical threshold filter to generate a gradient-orientation map for damage visualization. The proposed algorithm was capable of producing distinctive damage patterns when tested experimentally on a 3-mm aluminum plate with multiple simultaneous simulated defects. Compared to conventional techniques like local wavenumber estimation, the generation of the accumulated orientation map involves no filtering process in the frequency or wavenumber domain, at the expense of more accurate shaping of the defect. A spatial covariance analysis was adopted to locate damage from the results as well as to evaluate the correlation between different kinds of defects. Combining the proposed approach with conventional laser ultrasonic imaging techniques enables a fast and robust damage identification and characterization process which requires lower computational burden and practical operation.

Keywords

Guided waves, ultrasonic wavefield imaging, laser ultrasonic, non-destructive evaluation, spatial gradient analysis, Covariance matrix

Introduction

Ultrasonic guided waves propagating in plate-like structures, known as Lamb waves, have shown great potential in NDE-SHM applications due to their long propagation capacity and sensitivity to various defects.[1–4] Among the many both sparse and dense array interrogation architectures, laser ultrasonic techniques based on ultrasonic guided wave propagation are very useful because they provide full-field ultrasonic wavefield data with high spatial-temporal resolution for the purpose of ultrasonic wavefield imaging (UWI). Numerous contributions have been made to detect and visualize defects with various imaging techniques benefiting from the rich information provided by UWI data. Chia et al.[5] quantitatively evaluated the impact damage through a space-frequency analysis where the time domain signal recorded at each impinge point was Fourier transformed and arranged into 3D space-frequency tensor. The structural damage was visualized as concentrated spectral amplitudes by determining the spatial frame at the same frequency as the damage-related wave. In time-frequency analysis, Lee et al.[6] identified the debonding damage in a glass-fiber-reinforced plastic (GFRP) wind turbine blade with a wavelet-transformed ultrasonic propagation imaging method. The ultrasonic wave signal was converted into a 2D scalogram which contained the WT coefficient of all the frequency components of the time domain signal. The damage was detected by inspecting the transformed data on a frame-by-frame basis along the

Department of Structural Engineering, University of California San Diego, La Jolla, CA, USA

Corresponding author:
*Michael D Todd, Department of Structural Engineering, University of California San Diego, 9500 Gilman Drive, CA 92093-0085, USA.;
Email: mdtodd@eng.ucsd.edu*

time axis at one particular frequency. Furthermore, frequency and wavenumber analyses based on multi-dimensional Fourier transforms in space and time domains has continued to evolve.[7–9] Sohn et al.[7] visualized the delamination in composite structures with standing waves and Laplacian image filters in the wavenumber-frequency domain. Tian et al.[8] investigated a wave mode decomposition method with frequency-wavenumber analysis, which allows the acquisition of higher Lamb wave modes for early damage detection at shorter wavelength. Furthermore, Chang et al.[9] obtained the instantaneous wavenumber based on the Riesz transform to highlight the wavenumber change at the damaged area where the filtering process in the frequency-wavenumber domain was removed. Although these approaches provide multiple alternatives for damage feature extraction, the implementation of both spectral transforms and filtering processes highly relies on practical considerations and are often time-consuming and ad hoc.

Consequently, laser interrogation combined with signal processing methods that enable the efficient use of UWI data were desired to facilitate the damage detection process. The compressive sensing (CS) technique allows high-dimensional signals to be reconstructed from a sparse basis representation, which improves the scan time of current wavefield imaging.[10–12] However, the signal reconstruction efficiency highly depends on dictionary quality, and there can be high computational or data collection demands to obtaining the ”best” dictionary via supervised learning. In addition to above optimization approaches, Chong et al.[13] explored the potential of parameterizing the spatial scanning pattern instead of using a conventional raster scanning. Through a parametric curve scanning method according to the propagation patterns of guided waves, the curved incident and reflected wavefront could be tuned into a simple straight lines-like pattern in angle-radius (ϕ-R) domain. The UWI data stored in such polar coordinate space provides simpler patterns for frequency filtering methods and can be used as an alternative approach for sensing placement implementation. Chong et al.[14,15] estimated the phase and group velocities of A0 and S0 modes using the spatial covariance matrix. The approach not only was computationally efficient, but also minimized the information loss in comparison to the spectral transformation and other signal decomposition methods. The spatial covariance analysis demonstrated an approach to extract the dispersion curves of Lamb wave modes from the full-field ultrasonic data, that in turn provided a robust method to rapidly detect damage.

Beyond these features mined from the high-resolution UWI data, the potential of employing spatial gradient analyses for guided-wave damage detection has not been considered. In image recognition, the spatio-temporal gradient method is used to recognize a moving object in video data.[16] The similarity between image pairs can be measured through a correlation method based on the gradient orientation difference at each pixel.[17] In seismic applications, the spatial gradient of the seismic wavefield is analyzed to investigate important wave characteristics that can be directly related to wave propagation in layered earth.[18] Since the discontinuity of material properties at the damaged area is known to induce changes in the spatial ultrasonic waveform, it may then be reasonably surmised that such damage may be reflected by the change of spatial gradient field as time progresses.

This article proposes a laser ultrasonic imaging technique based on wavefield spatial gradients to visualize and characterize structural damage, taking advantage of the abundant spatial information contained in UWI data. Gradient vectors at each point are used as indicators of local waveform distortions induced by highly localized impedance changes in the damaged area. The derivation of the proposed method involves no frequency tuning or wave mode decomposition, which is computationally efficient and requires little manual operation in practice. Additionally, the process removes the complex wave patterns of guided waves and visually enhances the distortion caused by the defects for more intuitive identification and interpretation.

The rest of this article is organized as follows. The section ‘Laser Ultrasonic Interrogation System Configuration and Experimental Setup’ presents the laser ultrasonic techniques used to acquire the full-field ultrasonic wavefield data and the experimental setup. The obtained UWI data are stored in angle-radius (ϕ-R) domain through a circle scanning pattern which allows the implementation of the spatial covariance analysis for fast detection. Such UWI data in the polar coordinate space can be converted to Cartesian coordinates (X-Y) for more intuitive purposes. For comparison, a raster scanning is performed with identical experimental conditions because conventional laser ultrasonic imaging techniques are established on the UWI data stored in Cartesian domain. In section ‘Ultrasonic Wavefield Spatial Gradients’, the proposed wavefield spatial gradient analysis is elaborated step-by-step. Section ‘Results and Discussion’ introduces the simulated defects used in the experiment and presents the results on different defect scenarios. The damage pattern of the result indicates that each defect owns distinguishable scattering behavior in their spatial gradient field and the

uniqueness of each pattern can be observed quantitatively via their correlation in the covariance map. The result of local wavenumber estimation obtained from raster scanning is shown in the end of the section which illustrates several outstanding advantages of the proposed technique. Lastly, the conclusions of this study and pathways for ongoing work are summarized in the last section.

Laser Ultrasonic Interrogation System Configuration and Experimental Setup

Laser Ultrasonic Interrogation System Configuration

Figure 1(a) shows the schematic diagram of a laser ultrasonic interrogation system (LUIS), which comprises of a laser scanning system incorporated with a signal conditioning device, a data acquisition (DAQ) module, a contact sensor, and a computer used for signal processing and operation control. The laser scanning system in Figure 1(b) presents a two-dimensional (2D) laser mirror scanner (LMS) and a diode-pumped solid-state Q-switched Nd:YAG laser. The Q-switched laser is composed of a laser controller and a laser head with an output beam of 527 nm wavelength and pulse repetition rates (PRR) of single-shot up to 1 kHz. The 2D LMS is used to synchronize the 2-axis galvanometer scanner with the Q-switched laser to maneuver the laser impinging point rapidly at a PRR with predefined 2D space coordinates (X, Y). In LUIS, the laser scanning system is developed with the capability of performing a scanning process based a programmable scanning path (e.g., traditional raster, a circle, etc.).

Throughout the scanning process, the laser pulse optically impinges at each scan point to generate an ultrasonic wave based on the thermoelastic principle, which then propagates as shown in Figure 2. The generated ultrasound is then conditioned in the in-line filter (signal-conditioning device) through a contact sensor. Subsequently, the filtered ultrasound is digitized in the DAQ module, which is synchronized with the laser scanning system by receiving a triggering signal from the laser controller at each laser pulse emitted. During the digitizing process, the ultrasound is sampled at sampling time interval T_S for total K number of data points (each sample point is denoted by the integer index i) and then stored. The digitizing process is repeated until the scanning process is completed. Upon the completion of the scanning process, the measured ultrasonic waves are reconstructed and represented in UWI.

The left-hand-side of Figure 2 shows that the full-field ultrasonic signals are generated and measured by the LUIS with $N \times M$ grid points based on the raster scan. These full-field ultrasonic data are then represented in a three-dimensional (3D) X-Y-T tensor, representing spatial x-direction, spatial y-direction, and time samples t, respectively. The 3D tensor is illustrated in a 3D image (right-hand-side of Figure 2). This 3D image is the representation of the full-field ultrasonic wave propagation imaging (UWI in this paper).

Experimental Setup

Figure 1(c) shows the inspection configuration of the plate with a PZT sensor mounted at the center of the rear scanning surface. The plate was a 3-mm thick aluminum plate and

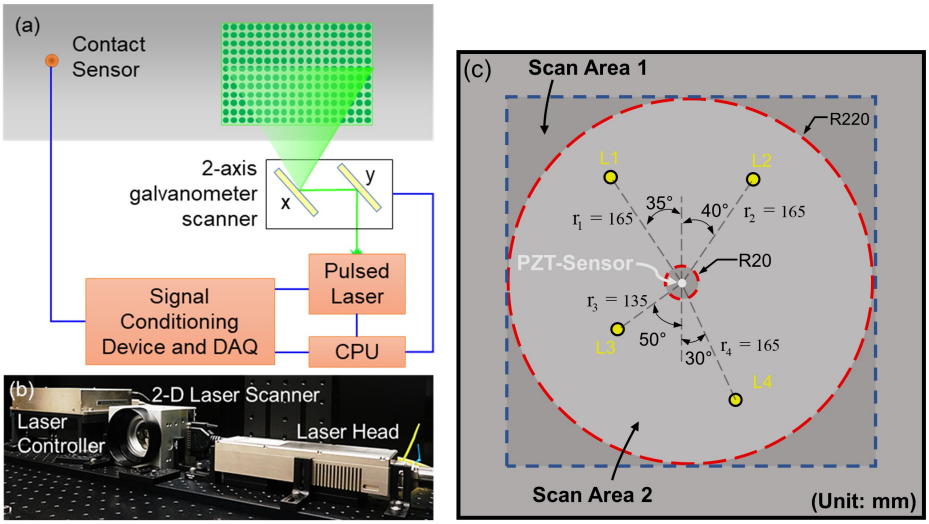

Figure 1. (a) Laser ultrasonic interrogation system, (b) laser scanning system, and (c) inspection configuration of a 3-mm aluminum plate.

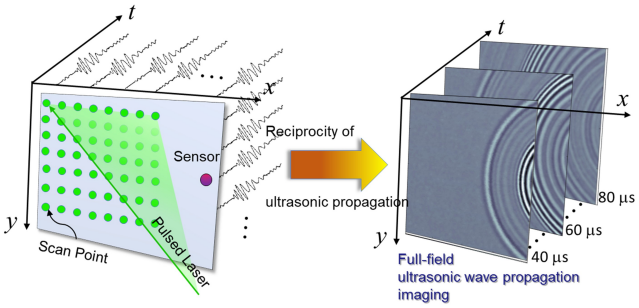

Figure 2. Full-field ultrasonic wave propagation imaging.

configured at a standoff distance of 1820 mm from the 2D LMS in this experiment setup. Four damage locations were considered in this paper and denoted as **L1**, **L2**, **L3**, and **L4** as indicated in the figure with the yellow circles.

Three different simulated defects on the 3-mm aluminum plate were designed and configured to evaluate the feasibility of the proposed gradient method (to be discussed in the next section), as shown in Figure 3 with the experimental materials and their relative positions to the plate from a top view. The first defect, denoted as **D1**, is a piece of 20×20 mm^2 plasticine attached at the rear scanning surface of the plate which is acted as a damper to attenuate the ultrasonic guided wave energy along its path. The second defect, denoted as **D2**, is a metallic screw, and the tip of the screw was polished flat and bonded to the rear scanning surface by cyano-acrylate based glue. The 5-mm diameter circular contact area between the tip of the screw and the surface of the plate was simulated as the source of the scattering wave from the reflected wave after the first guided wave propagating to the screw head. Third defect, denoted as **D3**, is the delaminated surface area (20×13 mm^2) simulated by an aluminum strip of 0.025-mm-thickness and 13-mm-width feeler gage. During the bonding process, a 20 mm-wide Teflon sheet was sandwiched between the surface of the plate and strip to prevent a 20×13 mm^2 area from being properly bonded.

In this article, three simulated damage cases with the defects (**D1**-**D3**) at the specific locations (**L1**-**L4**) as shown in Figure 1(c) were considered. Firstly, a single damage case was conducted where each defect was set and tested individually at corresponding locations. After that, a multi-location damage case was considered with three pieces of plasticine set at locations **L1**, **L2**, and **L4** simultaneously. To compare the defect-to-defect correlation with the spatial covariance analysis,[14] the plasticine at **L1** was replaced by a metallic screw while keeping the rest of the conditions unchanged. Lastly, a multi-type damage case was studied by including all three types of defects located at **L1**, **L2**, and **L3**, respectively.

Two separate full-field ultrasonic measurements based on a raster scan and a circle scan were carried out in different areas on the aluminum plate as shown in Figure 1(c). The first full-field measurement, referred to Scan Area 1, was performed based on the raster scanning method as indicated by the blue-dotted square with a side length of 440 mm. The second full-field measurement, referred to Scan Area 2, was performed based on the circle scanning method as indicated by the red-dotted circle with an inner radius of 20 mm and an outer radius of 220 mm. All measured ultrasonic signal in both full-field measurements was filtered in the in-line bandpass filter with the low cutoff-frequency of 50 kHz and the high cutoff-frequency of 500 kHz for the simulated damage cases. In Scan Area 1, the scanning range was set from -220 mm to 220 mm with an interval of 0.5 mm in both height and width directions, which made the total points in both x and y directions $M, N = 880$. The total sample number K was set to 2000 at a sampling interval of T_S = 0.1 μs. The UWI data obtained from the raster scanning was used to perform local wavenumber estimation

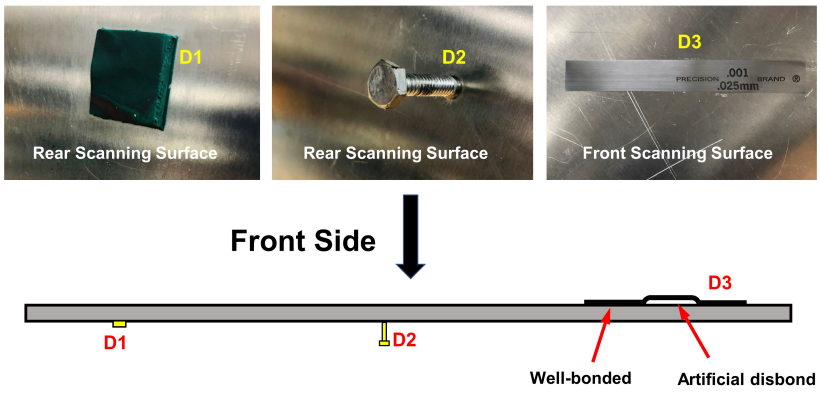

Figure 3. Artificial structural defects for simulating different impacts.

(LWE) in section 'Local Wavenumber Estimation' to use as a benchmark to evaluate the results of the proposed method in this paper. In Scan Area 2, the full-field ultrasound was measured and represented in a polar coordinate space with a three-dimensional *R*-ϕ-*T* tensor, representing spatial radius, circumferential angle, and time sample *t*, respectively. The scanning range for the circle scan was set with the radius from 20 mm to 220 mm at an interval of 1 mm. Then, the circumferential angle ranging was set from 0° to 360° at an interval of 0.78°. With these circle scanning settings, the total points in the radial direction was determined to be $M = 201$, and the total of scanned points in angular direction was determined at $N = 460$. As with the raster scanning, the total sample number *K* was set to 2000 at the sampling interval of $T_S = 0.1$ μs.

Although the full-field ultrasonic data of the Scan Area 2 were obtained in the polar coordinate (R, ϕ) space, these 2D waveforms still can be converted and represented in Cartesian coordinates (X, Y) by the standard transformations $X = R\cos\phi$ and $Y = R\sin\phi$. For example, Figure 4(a) shows a snapshot of the wavefield image in the *R*-ϕ domain at 50 μs. Then, after converting the *R*-ϕ domain to the *X*-*Y* domain, the ultrasonic wave propagation is intuitively interpreted in 2D space as shown in Figure 4(b).

Ultrasonic Wavefield Spatial Gradients

Spatial Gradient Image Construction

This section introduces the process of constructing the gradient map for damage identification from the full-field ultrasonic data stored in the *R*-ϕ-*T* tensor. Since the UWI data is formed in the 3D space-time domain, the 2D frame in space domain containing the intensity (normally equivalent to the amplitude of the ultrasonic wave) at each scanning point can be determined for a given time point. Letting the symbol U denote the intensity of wavefield in a space-domain frame, the image at any time point (denoted as *i*-index) along the time axis $i \in T$ can be represented as $\{U\}_i^{N\times M} \in \mathbb{R}^{N\times M}$ with N rows and M columns corresponding to the dimensions defined by total inspection angular points and radial points ($N = 460$ and $M = 201$) as shown in Fig. 5(a). The proposed algorithm uses the spatial gradient vectors as indicators of the local waveform distortions induced by local impedance changes at boundaries and defects. To measure the time variations of gradient vectors, a spatial-gradient profile is first determined that contains the gradient vectors at each scanning point for each time frame. The vectors are fully characterized by two components, $\{G\}_{i,R}^{N\times M}$ and $\{G\}_{i,\phi}^{N\times M}$, calculated by taking spatial derivatives of the intensity at each pixel with respect to two coordinates in the R (horizontal) and ϕ (vertical) directions, respectively, in polar space, or

$$\{G\}_{i,R}^{N\times M} = \frac{\partial\{U\}_i}{\partial R}, \quad \{G\}_{i,\phi}^{N\times M} = \frac{\partial\{U\}_i}{\partial\phi}. \tag{1}$$

Letting $U_{j,k} \in \{U\}_i^{N\times M}$ represent for the intensity of pixel (j, k) in the spatial domain, a spatial scale factor d is designated as shown in Figure 5(b) which defines the neighborhood of pixels around the location (j, k) to estimate the partial derivatives. The size of this scale factor governs the usual trade-off between competing objectives of image spatial resolution (low d) and signal-to-noise (higher d). In this paper, the standard central difference value of $d = 2$ is chosen, considering the scanning interval and estimated size of experimental defects. Based on equation 1, the gradient-orientation and gradient-magnitude profiles for each time

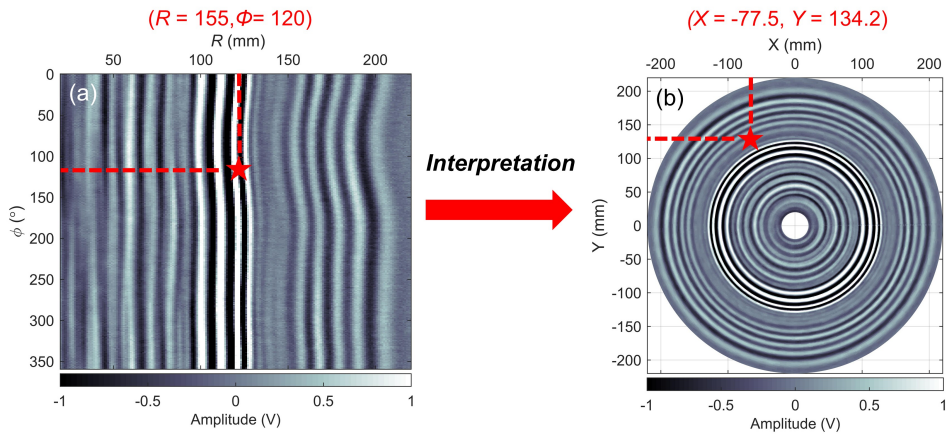

Figure 4. (a) Wavefield image stored in the *R*-ϕ domain at 50 μs, and (b) same wavefield image represented in *X*-*Y* domain.

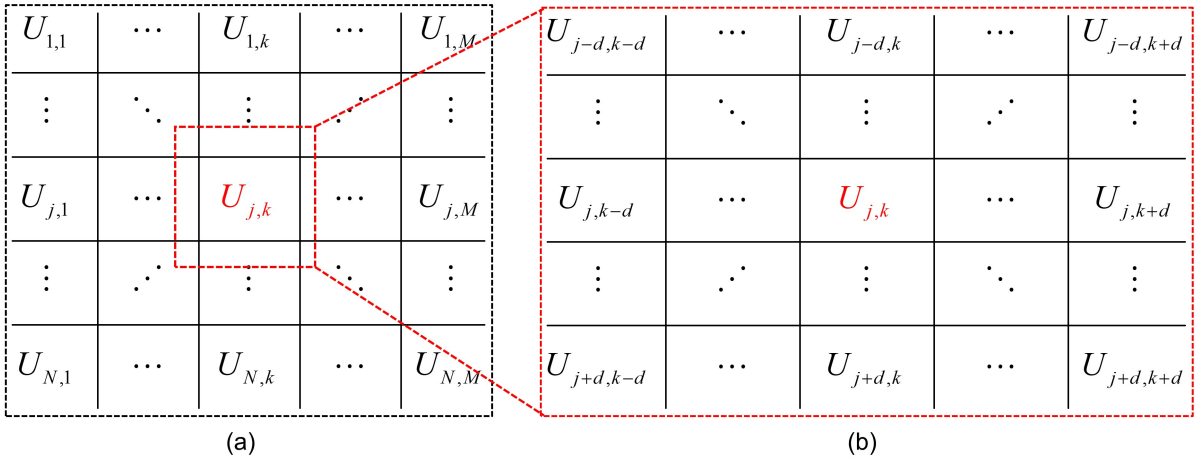

Figure 5. (a) 2D frame $\{U\}_i^{N\times M}$ for a given time point, (b) pixels defined by the scale factor d for location (j,k).

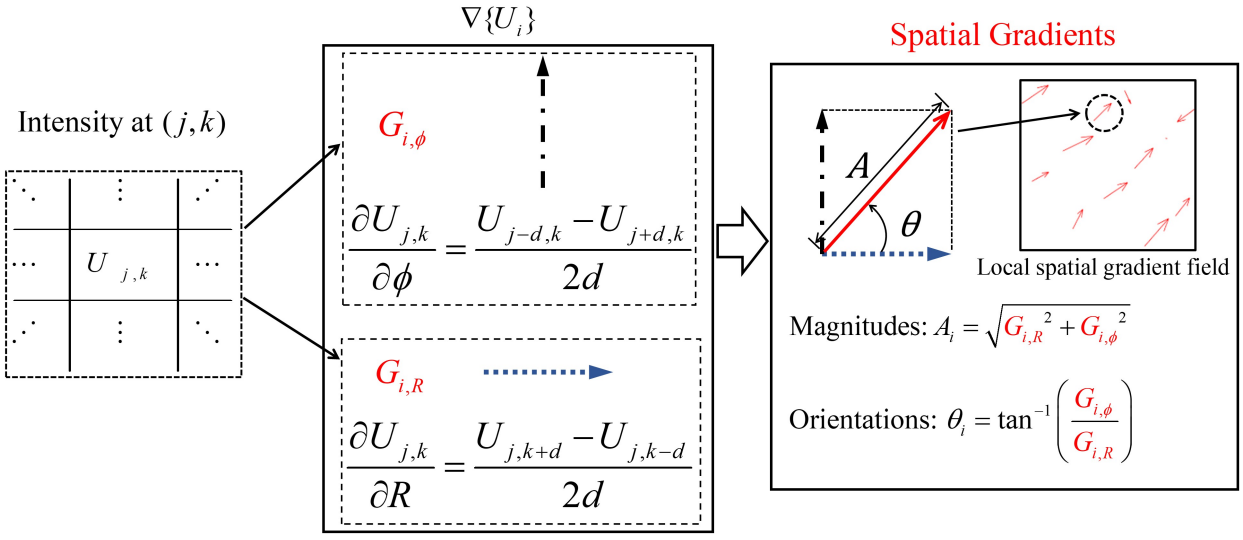

Figure 6. Flow diagram of spatial gradient analysis.

frame, $\{\theta\}_i^{N\times M}$ and $\{A\}_i^{N\times M}$, are consequently calculated:

$$\{\theta\}_i^{N\times M} = \tan^{-1}\left(\frac{\{G\}_{i,\phi}}{\{G\}_{i,R}}\right), \quad (2)$$

$$\{A\}_i^{N\times M} = \sqrt{\{G\}_{i,R}^{\ 2} + \{G\}_{i,\phi}^{\ 2}}. \quad (3)$$

Figure 6 shows the workflow used to obtain the gradient-orientation and gradient-magnitude profiles from the spatial gradient analysis for any given point (j,k) where $A_i \in \{A\}_i^{N\times M}$ and $\theta_i \in \{\theta\}_i^{N\times M}$. The gradient-magnitude noise level will be estimated and modeled in the next section in order to decide a threshold value for a denoising process to control the sensitivity of the gradient-orientation profiles.

Statistical De-noising Process using Gradient Magnitude Statistics

As mentioned, gradient vectors are sensitive not only to local distortions of the waveform but also to noise. The effect of noise becomes non-negligible as the random rotation of the gradient vector obtained from the noisy data will amplify the gradient-orientation variation. Therefore, a magnitude-based filtering process is determined to minimize the vector variation caused by noise. The threshold process is carried out through a statistical method based on the generation of a noise map.[19] In the wavefield data from a test, a 3D noise tensor can be generated by mapping 1D ultrasonic signals of each pixel under a time length before the first arrival mode. In this paper, the noise tensor, denoted as $\{U\}_{noise}^{N\times M\times P}$, was obtained by collecting the intensities from all pixels before time = 10 μs, where P is the sample number ($460 \times 201 \times 100$ counts in total), considering the variability of noise in both spatial and temporal directions. The fundamental intensity noise was modeled as zero-mean Gaussian, which was experimentally verified in Figure 7(a), which shows the histogram of a representative pixel series compared to a best-fit Gaussian probability density

function with a estimated standard deviation σ and zero mean. Both components of spatial gradient, $\{G\}_{i,R}$ and $\{G\}_{i,\phi}$, remain zero-mean Gaussian with identical standard deviations, since they are just differences of Gaussian variables; the standard deviation of these differenced Gaussian variables is computed theoretically to be $\frac{\sigma\sqrt{1-\rho}}{\sqrt{2}d}$, where ρ is the correlation coefficient between the pixel intensities used to compute the gradient and d is as defined above. This formulation allows neighboring pixel noise to be correlated, and an experimental study found that $\rho \approx 0.1$ in these ultrasonic images; a more detailed correlation length model could be employed, but first-order global correlation captures the dominant effects, and further detailed statistical study is beyond the scope of the current work. From this, the probability density function of the gradient-magnitude $\{A\}_{noise}^{N\times M\times P}$ may be computed as a Rayleigh distribution as shown in Figure 7(b), with shape parameter $\frac{\sigma\sqrt{1-\rho}}{\sqrt{2}d}$, given that it is the square root of the sum of squares of two Gaussian variables:

$$p(A) = \frac{2Ad^2}{(1-\rho)\sigma^2} e^{-\frac{A^2 d^2}{(1-\rho)\sigma^2}}. \tag{4}$$

As Figure 7(b) shows, this analytically-calculated statistical model for the gradient-magnitude noise is very accurate, compared to the histogram of experimentally measured gradient-magnitude noise values in the histogram. Given this distribution of the gradient-magnitude noise, a threshold value A_T that establishes the critical noise value for the null hypothesis may be found for a given confidence level α,

$$\int_0^{A_T} \frac{2Ad^2}{(1-\rho)\sigma^2} e^{-\frac{A^2 d^2}{(1-\rho)\sigma^2}} dA = \alpha, \tag{5}$$

which results in a threshold given by $A_T = \sqrt{1-\rho}\sigma\sqrt{-\log(1-\alpha)}/d$. In this work, α was chosen to be 0.98; a comparison that illustrates how the result is affected by different such choices will be shown in section 'Results and Discussion'. In summary, the filtering process first determines the locations where the gradient-magnitudes are over the confidence-based threshold value A_T and then extracts the gradient-orientations at the corresponding locations to highlight the wavefield distortion. This statistical operation ensures that only the gradient vectors with a magnitude above this threshold value A_T will be retained in a data set; otherwise the corresponding gradient-orientation will be set to zero. The gradient-orientation profile after de-noising is represented with a prime symbol ($\prime$) as $\{\theta'\}_i^{N\times M}$.

Damage Imaging

In an isotropic homogeneous medium, the ultrasonic guided wave will propagate radially outward from the excitation point with a circumferentially-uniform waveform front. Because the wavefront arrives simultaneously in each angular direction, a circular scanning pattern can generate and store the UWI data with simple straight lines-liked patterns in a polar coordinate space (R-ϕ) as shown in Figure 3(a). In the local spatial gradient field shown in Figure 6, the discontinuity/irregularity caused by wavefront distortions can be visualized and measured as the change of gradient-orientation $\{\theta'\}_i^{N\times M}$ as time progresses. The variation is defined as the difference between two consequent gradient-orientation profile pairs after de-noising with the

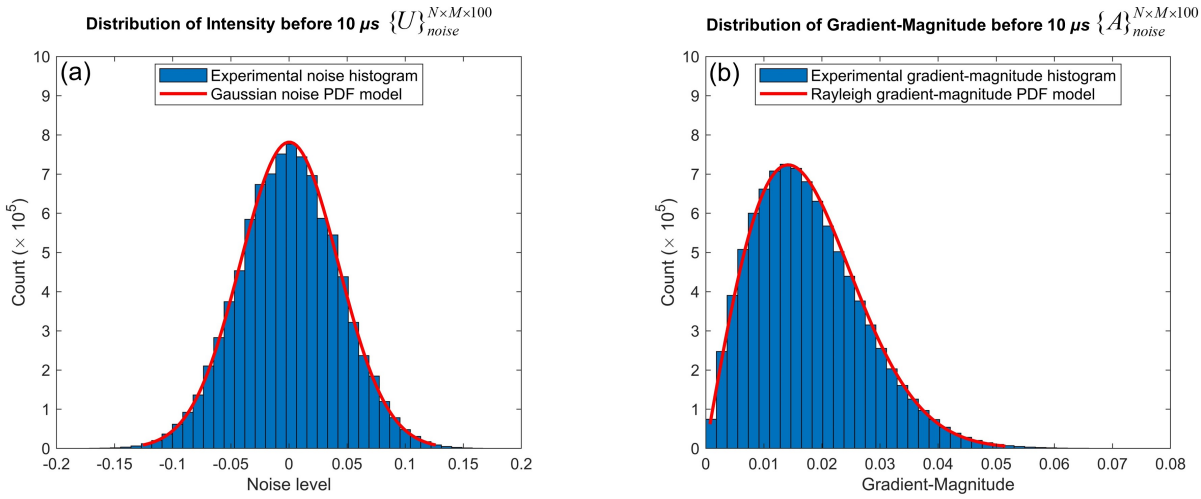

Figure 7. (a) Distribution of the pixel intensity noise, and (b) corresponding distribution of the gradient-magnitude noise.

time interval of T_S

$$\{\Delta\theta\}_i^{N\times M} = \mid \{\theta'\}_{i+1}^{N\times M} - \{\theta'\}_i^{N\times M} \mid . \quad (6)$$

It is natural to hypothesize that regions with different material properties or geometries may have significant gradient vector variation compared to adjacent undamaged areas, i.e., the local area affected by the defect would have a larger accumulated variation in its gradient-orientation map. Integrating the variation from starting time $i = 1$ to an endpoint $i = i_{end}$, the desired *gradient-orientation map* of the full-field ultrasonic wave is finally obtained for damage identification.

$$\{G\}_\theta^{N\times M} = \sum_{i=1}^{i_{end}-1} \{\Delta\theta\}_i^{N\times M}. \quad (7)$$

Ideally, the gradient-orientation map will indicate the damage location as the area with concentrated amplitudes (accumulation), while the undamaged area involving no waveform distortion will remain a randomized (and much more negligible) accumulation. However, despite sensitivity to the discontinuity of material properties caused by structural defects, spatial gradient vectors are also subjected to the local distortion of the waveform induced by reflected waves. The damage pattern located near the boundary of the plate in the resulting map will be overlaid by the presence of strong reflected waves. Because of this, a scanning result from averaged defect-free cases was pre-recorded from which a reference gradient-orientation map was determined denoted as $\{G\}_{\theta,0}^{N\times M}$,a reference or "baseline" state. Finally, then, the effect of the reflected wave may be removed by subtracting the baseline from the damaged data, or

$$\{G\}_{\theta,sub}^{N\times M} = \{G\}_\theta^{N\times M} - \{G\}_{\theta,0}^{N\times M}, \quad (8)$$

where the $\{G\}_{\theta,sub}^{N\times M}$ after baseline subtraction can be considered as the residual trajectories fully characterized by the defects. Subsequently, a damage localization process was developed to accurately locate the damage patterns observed in the resulting map $\{G\}_{\theta,sub}^{N\times M}$.

Damage Localization with Angle Covariance Matrix

For precise localization of the detected damage from the resulting gradient-orientation map $\{G\}_{\theta,sub}^{N\times M}$, a spatial covariance method recently developed[14,15] was used to determine the most likely angle in the radius-angle (R-ϕ) space for each damage. By defining a row vector $\boldsymbol{G}_n = (G_{n,1}, G_{n,2}, ..., G_{n,M}) \in \mathbb{R}^M$, the $N \times M$ matrix can be rewritten as

$$\{G\}_{\theta,sub}^{N\times M} = \begin{pmatrix} - & \boldsymbol{G}_1 & - \\ - & \vdots & - \\ - & \boldsymbol{G}_N & - \end{pmatrix} \in \mathbb{R}^{N\times M}, \quad (9)$$

with the covariance matrix of $\boldsymbol{G}_n$ is denoted as $\mathbf{C}_\Phi$ and expressed as

$$\mathbf{C}_\Phi = E[(\boldsymbol{G}_i - \bar{\boldsymbol{G}}_i)(\boldsymbol{G}_j - \bar{\boldsymbol{G}}_j)] \in \mathbb{R}^{N\times N}, \quad (10)$$

where $i, j = 1, 2, \cdots, N$, and $\bar{\boldsymbol{G}}_i$ and $\bar{\boldsymbol{G}}_j$ are the mean of each row vector $\boldsymbol{G}_n$. From the definition, the covariance matrix is symmetric along the diagonal values which are actually the variance of each angular set. Thus, the angle ϕ_d of the damage location to the center of the plate was firstly determined by localizing the point with largest variance along the angular direction, extracted from the diagonal values of the covariance matrix $\mathbf{C}_\Phi$. The radius of the damage location R_d was then determined by searching the maximal amplitude in the gradient-orientation map along the radius line at the angle ϕ_d obtained in previous step. Furthermore, the column elements at each ϕ_d were extracted for damage characterization which unveiled the correlation between various damage patterns when multiple defects presented themselves.

Results and Discussion

Single Location Damage Cases

The first single damage site case was conducted with the plasticine **D1** placed at **L1** shown in Figure 1(c) where the true angular and radial locations are known as $\phi_d = 125°$ and $R_d = 165$ mm. Figure 8(a) shows a snapshot of the original ultrasonic wavefield image at 60 μs when the incident A0 mode was propagating through the defect area in the red circle. The attenuated local waveform of the A0 mode affected by the plasticine are barely visible directly from the complex multi-modal wavefield. The corresponding covariance map $\mathbf{C}_\Phi$ shown in Figure 8(b) is still complex and thus hard for a person without any background to point out the angular value. Instead, the most likely angular location ϕ_d was determined from the diagonal values of the covariance matrix shown in Figure 8(c) with a minimum variance at $\phi_d = 125°$. The radial location R_d is hard to find due to the complex waveform along the Radius line 1 shown in Figure 12(a) extracted from the UWI with the polar coordinate space. Instead of using a single time frame for damage identification, the gradient-orientation

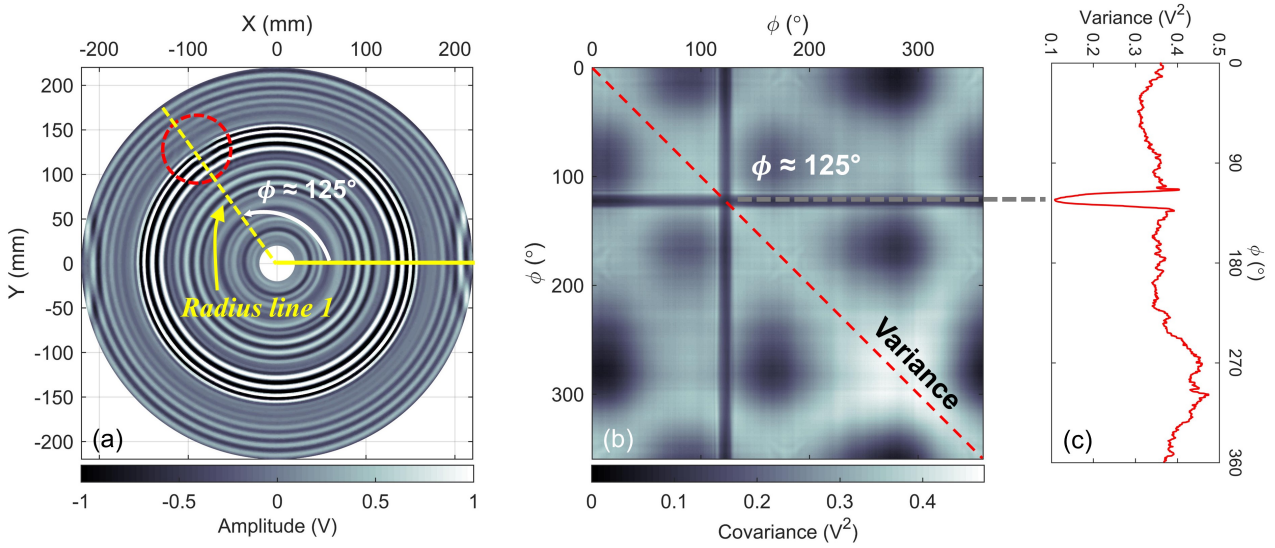

Figure 8. Single Damage Case with plasticine - (a) Ultrasonic wavefield image $\{U\}$ at 60 μs, (b) corresponding covariance map $\mathbf{C}_\Phi$, and (c) variance of each angle point.

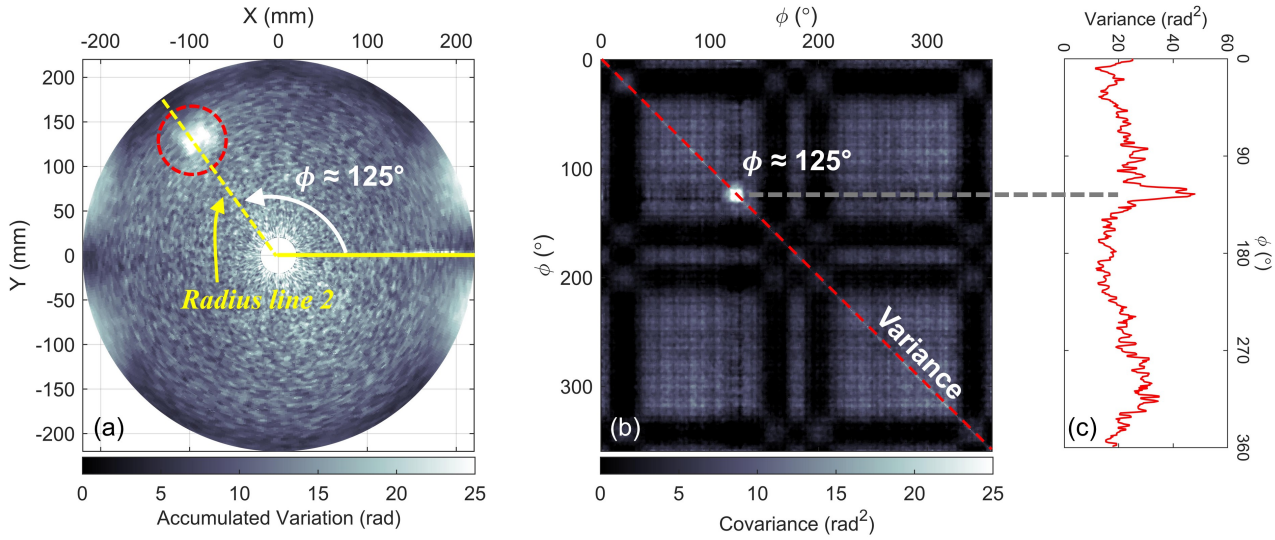

Figure 9. Single Damage Case with plasticine - (a) Gradient-orientation map $\{G_\theta\}$ at 60 μs, (b) corresponding covariance map $\mathbf{C}_\Phi$, and (c) variance of each angle point.

map proposed in this paper takes all the time frames before 60 μs into consideration, which shown in Figure 9(a), removes the complex wave patterns of guided waves and visually enhances the damage area. Besides, the covariance matrix of the result is much more intuitive as the angular location can be simply determined as the largest amplitude in the map shown in Figure 9(c) as $\phi_d = 125°$. In addition, the radial location in this case was accurately determined as $R_d = 164$ mm obtained from the largest amplitude along the radius line at $\phi_d = 125°$ shown in Figure 12(b). Compared to the true location of **L1**, the damage localization process can be considered as robust and computationally efficient.

However, even though the damaged location was detected in the gradient-orientation map with concentrated amplitudes of accumulated variation, the methodology was also sensitive to the propagating-back reflected wave which after the time of 60 μs distorted the consistency of guided waves and led to a higher accumulated amplitude in the undamaged area that near the boundary, as shown in Figure 10(a) at 75 μs. Figure 10(b) shows the false positives on the covariance map due to the reflected waves which increase the difficulty when determining the damage angular direction. Thus, the baseline subtraction method is unfortunately necessary when the structural defects are expected to be located near the boundary because of the presence of reflected waves.

Figure 11 shows that the gradient-orientation map is able to indicate the location of the damage at 80 μs although the reflected waves are strongly affecting the spatial waveform

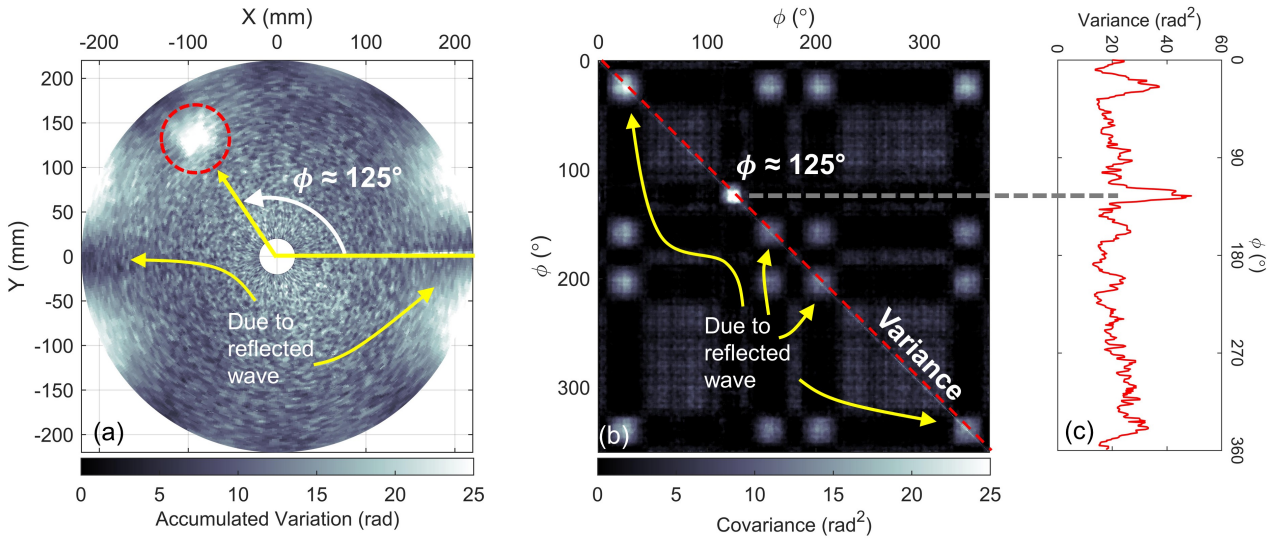

Figure 10. Single Damage Case with plasticine - (a) Gradient-orientation map $\{G\}_\theta$ at 75 μs with the presence of reflected wave, (b) corresponding covariance map $\mathbf{C}_\Phi$ with false positives, and (c) variance of each angle point.

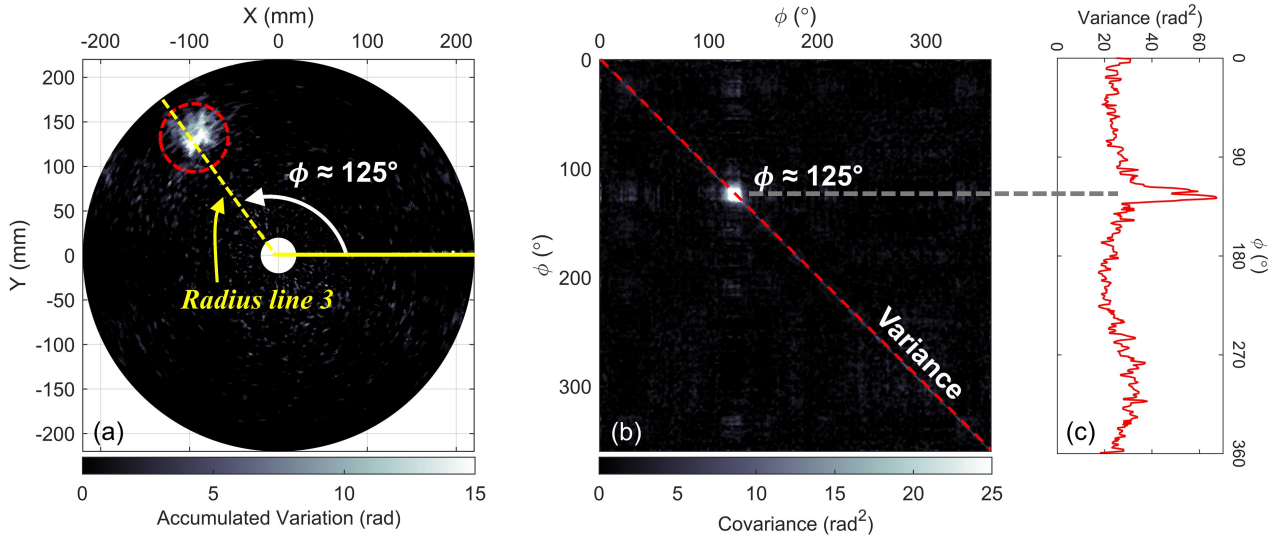

Figure 11. Single Damage Case with plasticine - (a) Gradient-orientation map at 80 μs with the baseline subtraction $\{G_{\theta,sub}\}$, (b) corresponding covariance map $\mathbf{C}_\Phi$, and (c) variance of each angle point with one clear maximum.

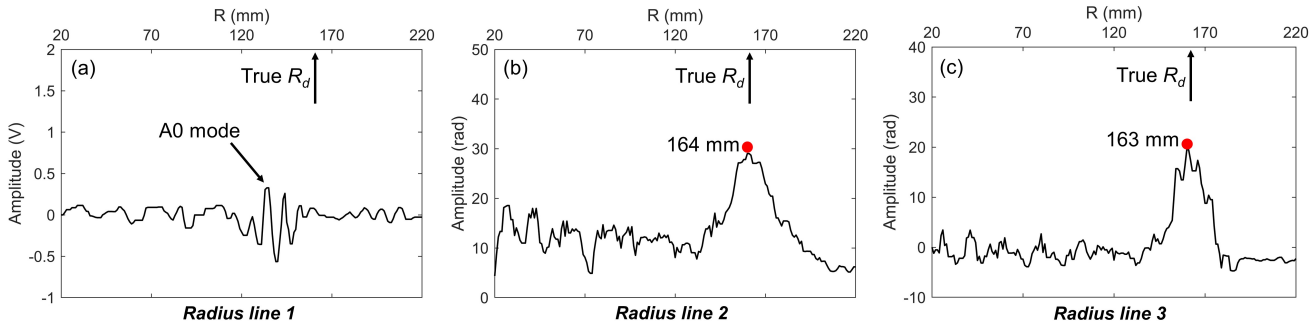

Figure 12. Single Damage Case with plasticine - (a) Radius line 1 from UWI $\{U\}$, (b) Radius line 2 from $\{G\}_\theta$, and (c) Radius line 3 from $\{G\}_{\theta,sub}$.

at several locations. With the baseline subtraction process, the "false positives" caused by the reflected wave in certain directions were eliminated which no longer hindered the accumulated variation caused by "true" defect. Besides, the

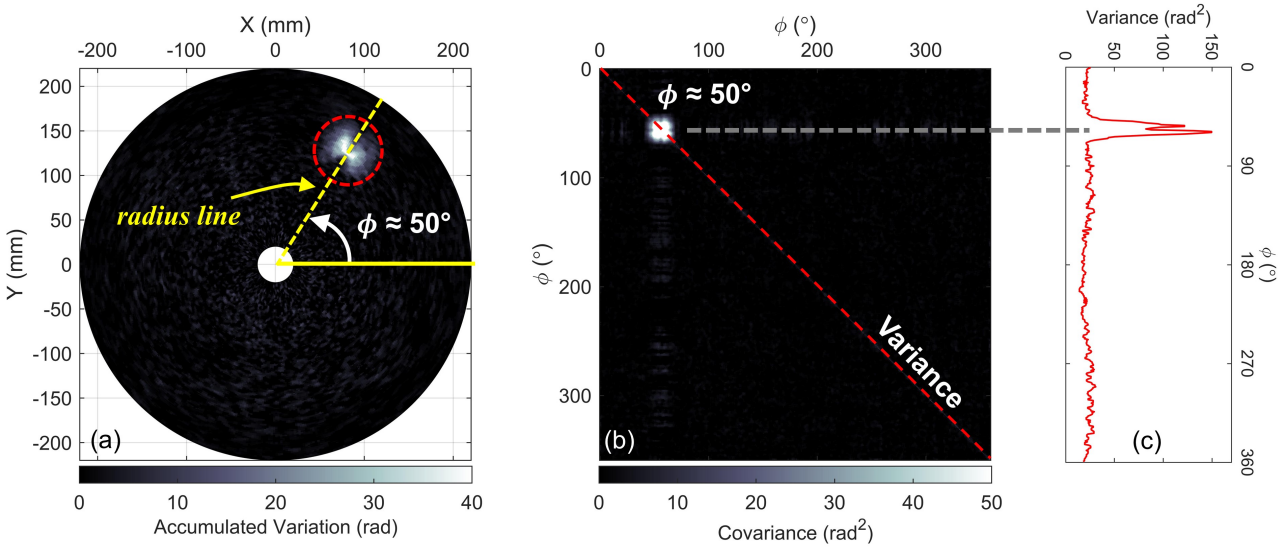

Figure 13. Single Damage Case with screw - (a) Gradient-orientation map $\{G\}_{\theta,sub}$ at 80 μs, (b) corresponding covariance map $\mathbf{C}_{\Phi}$, and (c) variance of each angle point.

quality of the resulting map is improved significantly and the local maximum is much clearer in the diagonal values of the covariance map. Following the same localization process, the angular and radial locations were determined as $\phi_d = 125°$ and $R_d = 163$ mm, which are also quite close to true values. For brevity, all the following results will show the orientation maps with baseline subtraction ($\{G\}^{N\times M}_{\theta,sub}$) and follow the same localization process for ϕ_d and R_d. With quick damage detection and localization, however, the size of structural defects like plasticine can not be determined clearly because the spatial gradient analysis focuses on the waveform inconsistency. Thus, the damage pattern failed to reveal the true dimension of plasticine, but precise characterization beyond localization is not the point of the current proposed method.

The proposed method was then tested with the screw **D2** at **L2** used for the second single-site damage case. Figure 13(a) shows the gradient-orientation map at 80 μs with a strong and clear damage pattern despite that the contact area between screw and plate is small (5 mm in diameter). The covariance map indicated the angular direction in Figure 13(b) which was then quantitatively determined from the diagonal values in Figure 13(c) as $\phi_d = 50°$. The radial location of the damage $R_d = 165$ mm was obtained from the largest value along the radius line at $\phi_d = 50°$. Similar to plasticine, the metallic screw as an excitation source induced extra waveform distortion around the damage area, which hindered the true size of the screw with an overestimated pattern in the resulting map.

For the third case of single-site damage **D3** at location **L3**, unlike the previous two defects, the gradient-orientation map in Figure 14(a) gives a distinct shape of the delamination. The angular direction is shown clearly in the covariance map and accurately determined from the diagonal values as $\phi_d = 220°$. The radial location of the damage $R_d = 132$ mm is obtained from the largest value along the radius line at ϕ_d.

Furthermore, the impact of different threshold values in the de-noising process to the damage pattern was demonstrated here where two more α values were set for comparison. With a lower α value in Figure 15(a), the shape of the defect is unclear and the whole area is contaminated by noise. With a higher value $\alpha = 0.9999$, the genuine (defect-related) signals were partially filtered out through the de-noising process, which led to an incomplete and inaccurate damage pattern. Because the surface delamination induces no waveform distortion outside the disbonded area, the size of defect can be visualized rather robustly with an appropriate α value.

Multi-Location, Single-Type Damage Case

In this case, three identical pieces of plasticine denoted as **D1** were attached at locations **L1**, **L2**, and **L4**. Similar to previous single-damage case, all three artificial defects were detected in a same gradient-orientation map clearly at the time 80 μs shown in Figure 16. From the diagonal values of the covariance matrix, the angular directions of three damages were determined as $\phi_d = 50°$, $125°$, and $310°$, respectively. The corresponding radial locations, $R_d = 163$, 162, and 160 mm, were again determined by extracting the radius lines at above angles. The three concentrated amplitudes observed in the off-diagonal area

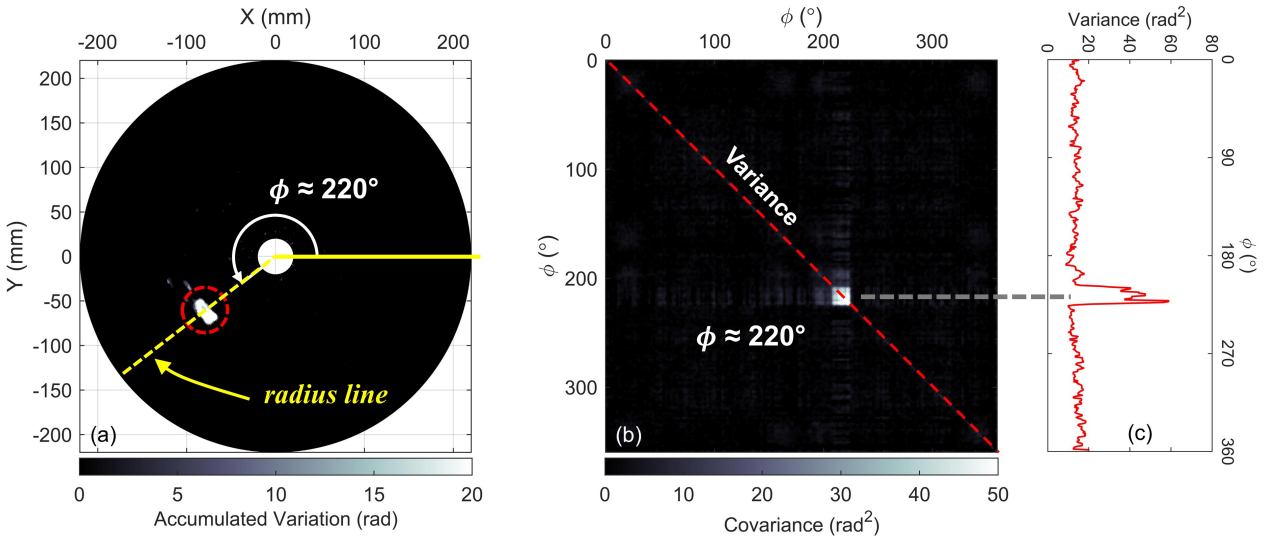

Figure 14. Single Damage Case with delamination - (a) Gradient-orientation map $\{G\}_{\theta,sub}$ at 80 μs, (b) corresponding covariance map $\mathbf{C}_{\Phi}$, and (c) variance of each angle point.

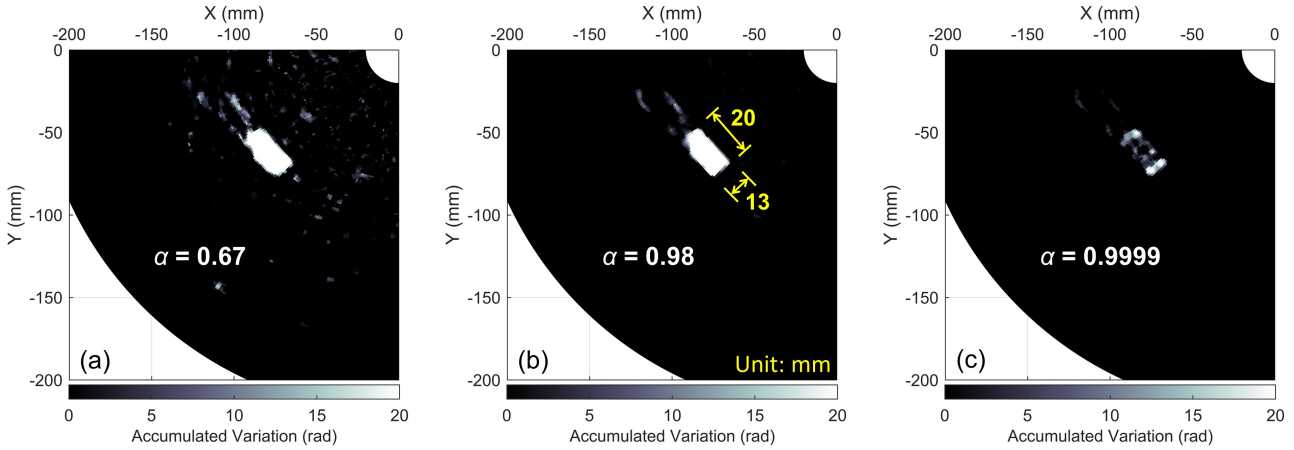

Figure 15. Damage pattern under different confidence level α - (a) $\{G\}_{\theta,sub}$ at 80 μs with α = 0.67, (b) $\{G\}_{\theta,sub}$ at 80 μs with α = 0.98, and (c) $\{G\}_{\theta,sub}$ at 80 μs with α = 0.9999.

of the covariance map (noted as strong correlation) revealed that same type of defects would result in high covariance between their angles due to their similarity in size and material properties.

To study such defect-to-defect correlation on the features, the plasticine at location **L1** was replaced by a screw (**D2**) while the plasticine at **L2** and **L4** remained unchanged. Because the damage patterns of structural defects like plasticine and screw through spatial-gradient analysis cannot reflect the true size with a precise shape, the gradient-orientation map shown in Figure 17(a) is highly similar compared to the previous result (Figure 16(a)). Furthermore, the variance of each angle does not change too much as shown in Figure 17(c). However, as observed in the covariance map, only one high-amplitude pattern presents in the off-diagonal area in this case. The covariance elements along each angle R_d, shown as the three yellow dashed lines in Figure 16(b) and Figure 17(b), were then extracted and compared simultaneously. Figure 18 plots three covariance lines at the three damage angles for the above two cases, respectively. Figure 18(a) with three same type defects (plasticine) proves that each defect is equally correlated to others as the covariance curves are similar. Oppositely, Figure 18(b) illustrates that the screw is only correlated to itself, while having almost zero covariance with the plasticine defects at the other two angles. Based on such results, the proposed technique provides not only quick

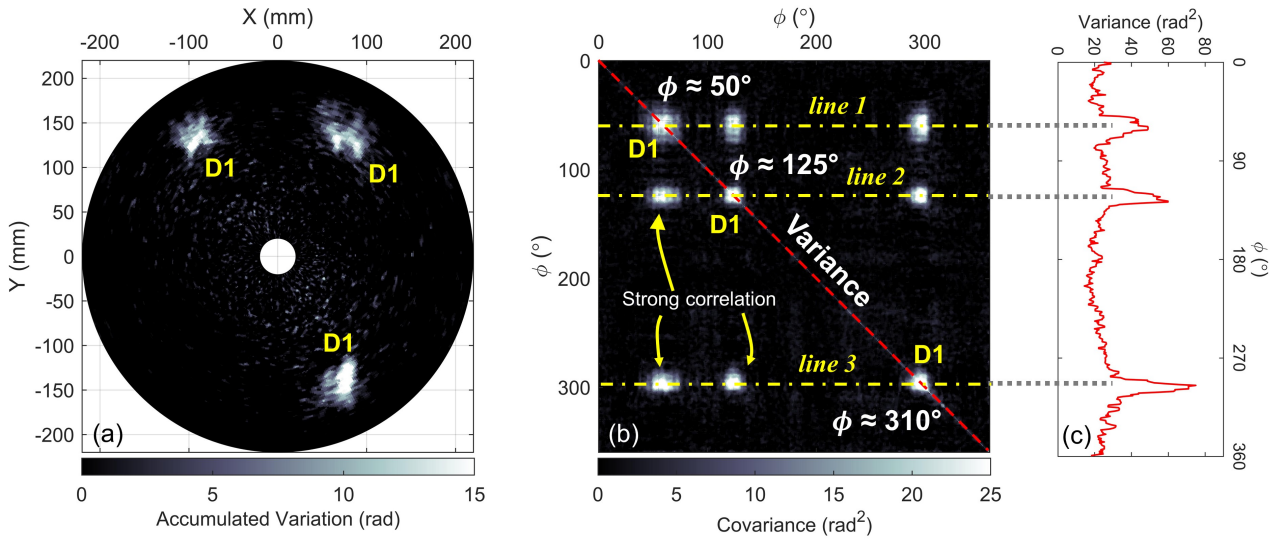

Figure 16. Multi-Location Damage Case with same type of defects - (a) Gradient-orientation map $\{G\}_{\theta,sub}$ at 80 μs, (b) corresponding covariance map $\mathbf{C}_{\Phi}$, and (c) variance of each angle point.

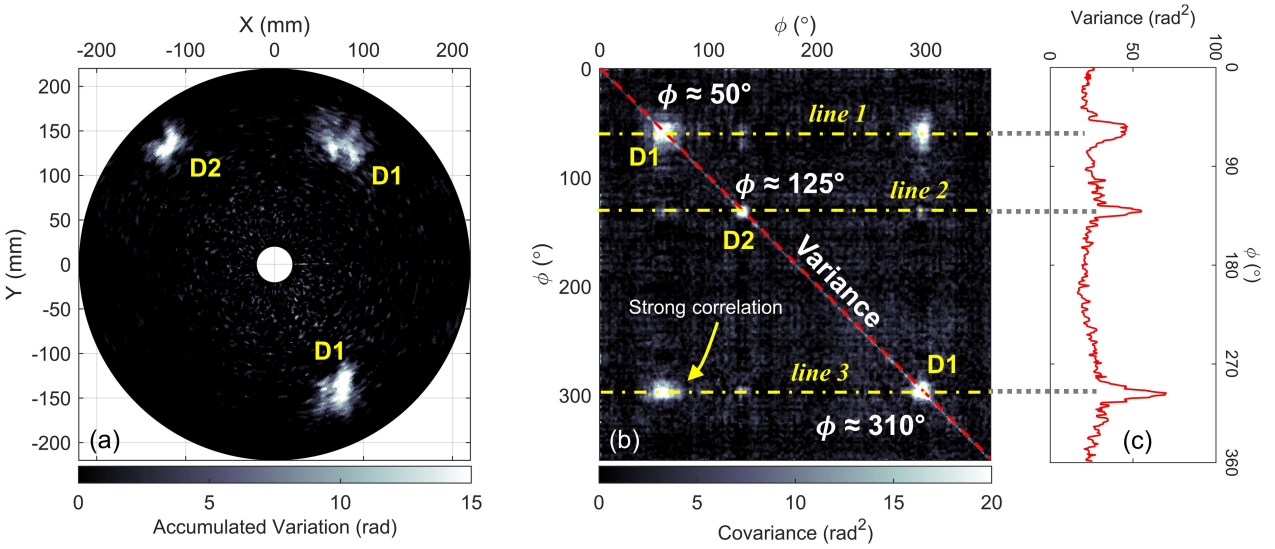

Figure 17. Multi-Location Damage Case with two types of defects - (a) Gradient-orientation map $\{G\}_{\theta,sub}$ at 80 μs, (b) corresponding covariance map $\mathbf{C}_{\Phi}$, and (c) variance of each angle point.

damage detection and localization but also suggests some level of classification as well.

Multi-Type Damage Case

The multi-type damage case, including all three types of scatterers **D1**, **D2**, and **D3** located at **L1**, **L2**, and **L3**, respectively, was conducted to evaluate both the detectability and sensitivity of the proposed method to various damage types. Similarly, all three artificial defects were detected in the gradient-orientation map $\{G\}_{\theta,sub}$ at 80 μs as shown in Figure 19(a). From the diagonal values of the covariance matrix, the angular directions of three damages were determined as $\phi_d = 50°$, $125°$, and $220°$ with radial locations $R_d = 164$, 160, and 132 mm. The pattern in covariance map validates the conclusion made in multi-location case that no correlation appears at the off-diagonal area when the defects share little similarity. For a more intuitive comparison, the three covariance lines for each damage angular location ϕ_d, denoted as lines 1, 2 and 3 in Figure 19(b), were again extracted and plotted in Figure 20 where only large amplitudes concentrated at the angular point itself are observed.

Local Wavenumber Estimation

In this paper, the local wavenumber[20] was estimated as a conventional frequency-wavenumber based imaging technique for comparison. A raster scanning process was performed on a same multi-type damage case including

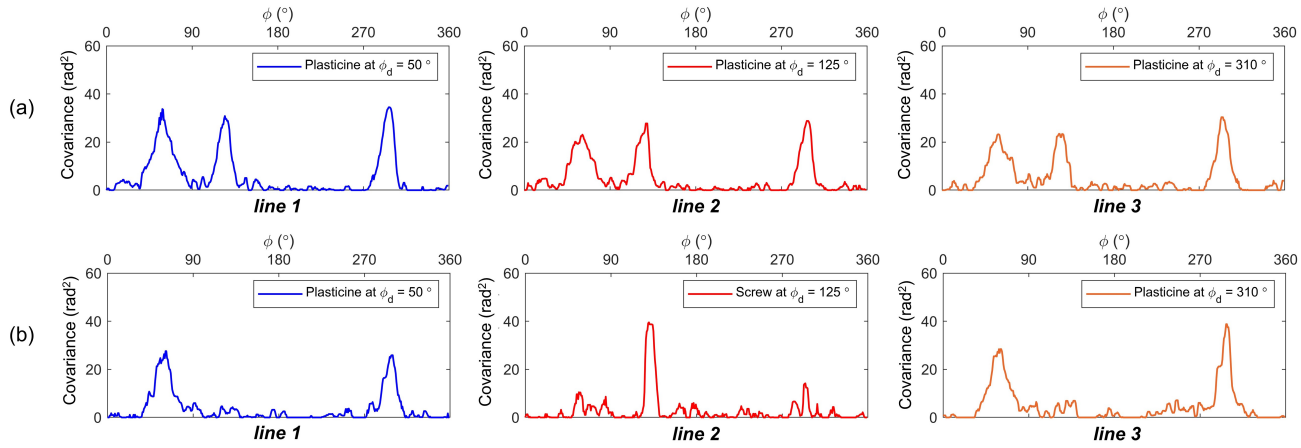

Figure 18. (a) The covariance lines with same type of defects, and (b) the covaraince lines with two different types of defects.

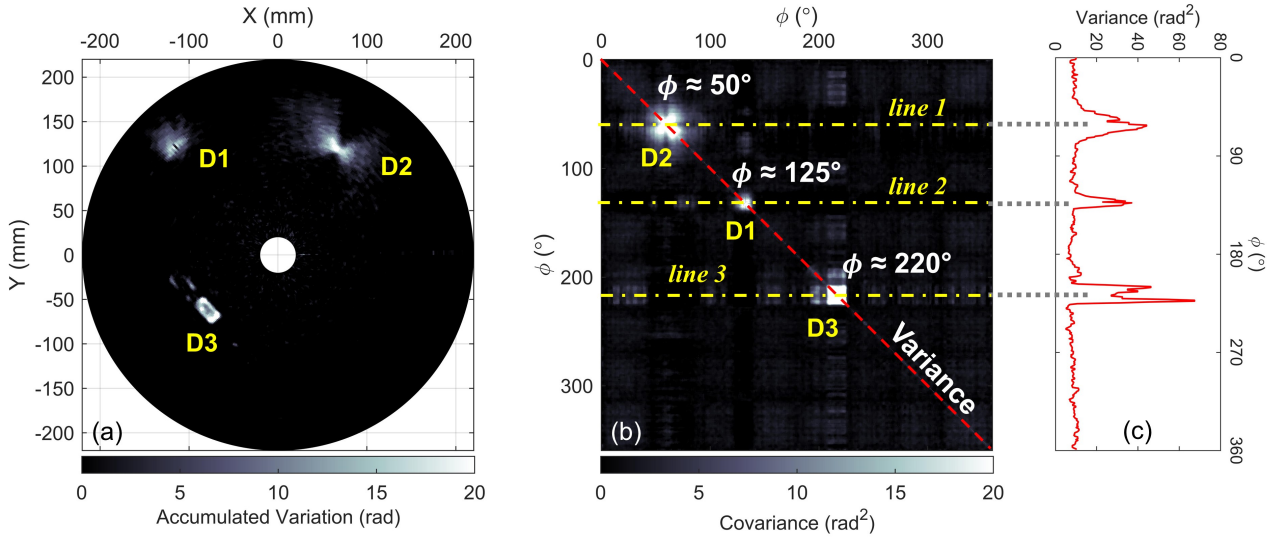

Figure 19. Multi-type Damage Case - (a) Gradient-orientation map $\{G\}_{\theta,sub}$ at 80 μs, (b) corresponding covariance map $\mathbf{C}_\Phi$, and (c) variance of each angle point.

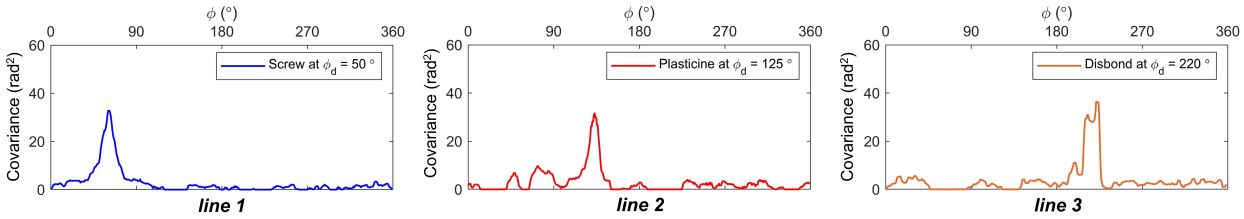

Figure 20. The covariance lines at each angle for multi-type damage case.

all three types of defects in section 'Multi-Type Damage Case' which generated and stored the UWI data in *X-Y-T* described in section 'Experimental Setup'. The frequency-wavenumber spectrum was first obtained through the 3D Fourier transform of the *X-Y-T* tensor to isolate wave modes. A0 mode was selected in this case by estimating the corresponding frequency-wavenumber curve with a curve fitting method. Given a center frequency f_c, the center wavenumber k_c was subsequently calculated by solving the fitting $f-k$ curve. A frequency bandpass filtering process was performed based on the selected f_c with a Gaussian-shaped window. The resulting single-mode and frequency-narrowband data were then passed through a wavenumber bandpass filter bank parameterized by corresponding center wavenumber k_c. After enveloping and summing the inverse Fourier transform to the filtered data across time, the desired local wavenumber estimate map was obtained.

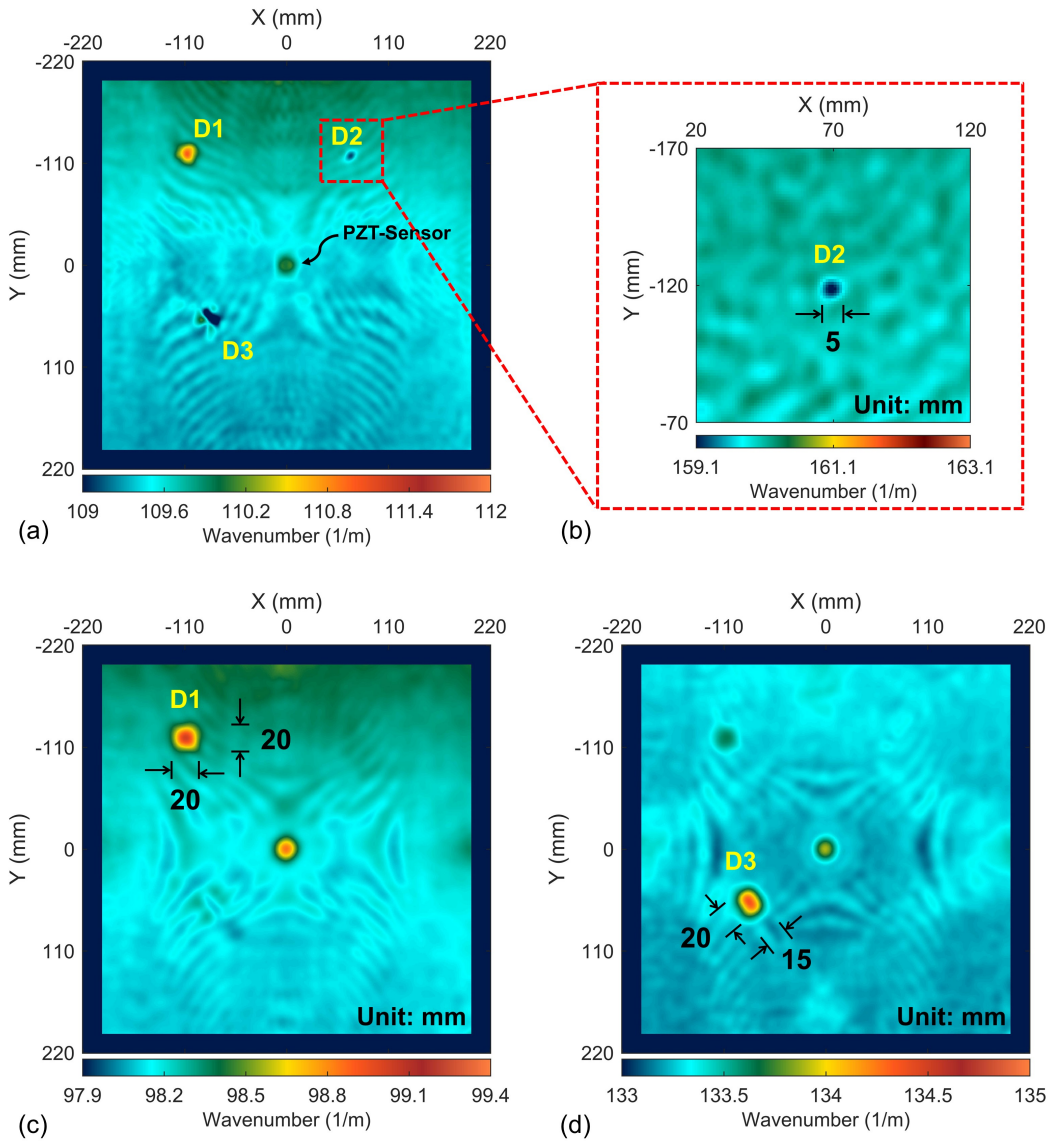

Figure 21. Local wavenumber estimate - (a) Three defects under $f_c = 200$ kHz, (b) screw **D2** under $f_c = 215$ kHz, (c) plasticine **D1** under $f_c = 150$ kHz, and (d) delamination **D3** under $f_c = 145$ kHz.

With a selected center frequency $f_c = 200$ kHz in Figure 21(a), the locations and relative sizes of three defects were detected in one map. A different colormap was used to show the results following the results of the original paper. However, finding the true shape of the defect requires a time-consuming frequency tuning process, because different defects are only sensitive to certain frequency ranges related to their boundary sizes. With a center frequency f_c = 215 kHz, 150 kHz, and 145 kHz, the defects **D2**, **D1** and **D3** were observed with more precise shapes (shown in Figure 21(b), (c), and (d), respectively). Additionally, the transducer located in the center of the plate appeared in the map as a "false positive" pattern through damage identification which is sometimes misleading and may affect the center frequency selection. Such effect of the transducer can be significantly reduced with the circle scanning process used in this paper by selecting a radial range that excludes the transducer.

Compared to the local wavenumber estimation, the proposed method can be used as a quick damage detection and localization technique, which minimizes the information loss through the spectrum transform and requires little manual operation and computational burden. Additionally, the pattern of delamination in the gradient-orientation map is believed to be more accurate while the shape in the local wavenumber estimate map has a less-distinct boundary. Although the shape of damaged area caused by the scatterers in this work can not be reflected from the map directly, the covariance map technique is proven to be an efficient tool to identify different defects with their correlation through the spatial covariance analysis.

Conclusion

In this paper, laser ultrasonic imaging of the wavefield spatial gradients was proposed for damage visualization and localization. By monitoring the accumulated variation in the gradient vector field, a gradient-orientation map was generated with distinctive damage patterns. The proposed method was tested on the ultrasonic wavefield imaging obtained from a 3-mm aluminum plate with several configurations of artificial damages. The residual gradient-orientation map showed the ability to detect various damage types under the impact of reflected waves. The diagonal of variances at each angle point in the covariance matrix of the results was firstly used to for damage localization in the angular direction. The radial location was then determined as the local maximum in the radius line at the corresponding angle. For the multiple-damage cases, the covariance lines at each angle were extracted which indicated the similarity (defect-to-defect correlation) between different types of defects. Compared with conventional techniques, the proposed methodology requires less "engineering judgment" and is computationally much more efficient. Additionally, the spatial vectors appear to be a good indicator of defects like delamination with a high-quality damage image in the gradient-orientation map. When dealing with potential defects that scatter similarly to the plasticine and screw used herein, the proposed technique can be used as a fast and robust damage detection and localization method. The local wavenumber estimation with a high-resolution raster scan can be performed around located the damage area which will significantly facilitate the scanning process. The use of this technique on highly anisotropic materials is an important consideration for future work, likely involving parametric rather than circular scanning and optimization, beyond the scope of the current paper.

Declaration of conflicting interests

The authors declared no potential conflicts of interest with respect to the research, authorship, and/or publication of this article.

Acknowledgements

The authors acknowledge funding from UC Office of the President for support of this work.

References

1. Worlton D. Ultrasonic testing with lamb waves. Technical report, General Electric Co., Hanford Atomic Products Operation, Richland, Wash., 1956.
2. Rose JL. A vision of ultrasonic guided wave inspection potential. In *Proceedings of the 7th ASME NDE Tropical Conference-2001*.
3. Rose JL. The upcoming revolution in ultrasonic guided waves. In *Nondestructive Characterization for Composite Materials, Aerospace Engineering, Civil Infrastructure, and Homeland Security 2011*, volume 7983. International Society for Optics and Photonics, p. 798302.
4. Yuan FG. *Structural health monitoring (SHM) in aerospace structures*. Woodhead Publishing, 2016.
5. Chia CC, Lee JR and Park CY. Radome health management based on synthesized impact detection, laser ultrasonic spectral imaging, and wavelet-transformed ultrasonic propagation imaging methods. *Composites Part B: Engineering* 2012; 43(8): 2898–2906.
6. Lee JR, Chia CC, Shin HJ et al. Laser ultrasonic propagation imaging method in the frequency domain based on wavelet transformation. *Optics and Lasers in Engineering* 2011; 49(1): 167–175.
7. Sohn H, Dutta D, Yang JY et al. Delamination detection in composites through guided wave field image processing. *Composites science and technology* 2011; 71(9): 1250–1256.
8. Tian Z and Yu L. Lamb wave frequency–wavenumber analysis and decomposition. *Journal of Intelligent Material Systems and Structures* 2014; 25(9): 1107–1123.
9. Chang HY and Yuan FG. Damage imaging in a stiffened curved composite sandwich panel with wavenumber index via riesz transform. *Structural Health Monitoring* 2020; 19(3): 902–916.
10. Di Ianni T, De Marchi L, Perelli A et al. Compressive sensing of full wave field data for structural health monitoring applications. *IEEE transactions on ultrasonics, ferroelectrics, and frequency control* 2015; 62(7): 1373–1383.
11. Harley JB and Chia CC. Statistical partial wavefield imaging using lamb wave signals. *Structural Health Monitoring* 2018; 17(4): 919–935.
12. Park B, Sohn H and Liu P. Accelerated noncontact laser ultrasonic scanning for damage detection using combined binary search and compressed sensing. *Mechanical Systems and Signal Processing* 2017; 92: 315–333.
13. Chong SY and Todd MD. Parameterization of spatial ultrasonic wavefront via laser ultrasonic technique. *Structural Health Monitoring 2019* 2019; .
14. Chong SY and Todd MD. Dispersion curve estimation via a spatial covariance method with ultrasonic wavefield imaging. *Ultrasonics* 2018; 89: 46–63.
15. Chong SY and Todd MD. Statistical damage detection based on full-field covariance of circumferential scan ultrasonic measurement. In *Health Monitoring of Structural and*

Biological Systems XII, volume 10600. International Society for Optics and Photonics, p. 106002J.

16. Liou SP and Jain RC. Motion detection in spatio-temporal space. *Computer Vision, Graphics, and Image Processing* 1989; 45(2): 227–250.
17. Zhao M, Yuan Y, Li B et al. A new feature extraction model based on image gradient. In *2013 6th International Congress on Image and Signal Processing (CISP)*, volume 1. IEEE, pp. 390–394.
18. Van Renterghem C, Schmelzbach C, Sollberger D et al. Spatial wavefield gradient-based seismic wavefield separation. *Geophysical Journal International* 2018; 212(3): 1588–1599.
19. Chong SY, Lee JR and Park CY. Statistical threshold determination method through noise map generation for two dimensional amplitude and time-of-flight mapping of guided waves. *Journal of Sound and Vibration* 2013; 332(5): 1252–1264.
20. Flynn EB, Chong SY, Jarmer GJ et al. Structural imaging through local wavenumber estimation of guided waves. *Ndt & E International* 2013; 59: 1–10.